TRIPLE FREQUENCY RADAR REFLECTIVITY SIGNATURES OF SNOW: OBSERVATIONS AND COMPARISONS TO THEORETICAL ICE PARTICLE SCATTERING MODELS

by

Michael J. Hiley

A thesis submitted in partial fulfillment of

the requirements for the degree of

Master of Science

(Atmospheric and Oceanic Sciences)

at the

UNIVERSITY OF WISCONSIN-MADISON

2012

APPROVED: _____ DATE: _____

Dr. Ralf Bennartz, Academic Advisor

ABSTRACT

An observation-based study is presented that utilizes aircraft data from the 2003 Wakasa Bay AMSR Precipitation Validation Campaign to assess recent advances in the modeling of microwave scattering properties of realistic ice particles in the atmosphere. Previous work has suggested that a triple-frequency reflectivity framework appears to have utility for identifying key microphysical properties of snow, potentially providing much-needed constraints on significant sources of uncertainty in current active microwave snowfall retrieval algorithms. However, these results were based solely on a modeling framework. In contrast, this study considers the triple-frequency approach from an observational perspective using airborne radar observations from the Wakasa Bay field campaign. After accounting for several challenges with the observational dataset, such as beam mismatching and attenuation, observed dual wavelength ratio (DWR) results are presented that confirm both the utility of a multi-frequency approach to snowfall retrieval and the validity of the unique signatures predicted by complex aggregate ice particle scattering models. This analysis provides valuable insight into the microphysics of frozen precipitation that can in turn be applied to more readily available single and dual-frequency systems, providing guidance for future precipitation retrieval algorithms.

1. INTRODUCTION

The ability to accurately quantify snowfall is critical for various reasons. A significant portion of precipitation at middle and high latitudes falls as snow (Liu 2008a, Hiley et al. 2011), and thus high-resolution knowledge of the temporal and spatial variability of snowfall is crucial for water cycle considerations, as well as quantifying the impacts of climate change at high latitudes where changes are already particularly evident (Hinzman et al. 2005, Luckman et al. 2006, Choi et al. 2010). The most promising method for achieving the desired resolution is via remote sensing methods, particularly space-borne active and passive microwave sensors. Much work has been accomplished in the field of microwave remote sensing of ice clouds and frozen precipitation; however, large retrieval uncertainties remain (Hiley et al. 2011). These uncertainties arise from the inability to directly measure various critical microphysical parameters, such as snow size distribution (SSD), mass-size relationships of frozen hydrometeors, particle fall speeds, and ice particle shape.

Compared to liquid cloud and rain drops, ice clouds and snowflakes are difficult to study due to their complex geometry. Ice crystal habits can vary from simple pristine needles and hexagonal plates to complex dendrites, as well as aggregates of multiple snowflakes. These different ice habits can have significantly different microwave scattering properties, and no reliable method to explicitly determine ice habit from active or passive microwave sensors currently exists. Therefore assumptions about ice habit and corresponding scattering properties must be made which result in large uncertainties in key derived parameters such as ice water content (IWC) and liquid equivalent snowfall rate.

In quantifying these scattering properties of ice, investigators have often used spherical particles consisting of a mixture of air and ice with a specified overall density (e.g., Bennartz and Petty 2001; Liu 2004). This methodology was useful because it allowed for the explicit calculation of scattering properties from Mie theory. Intuitively, this seems an over-simplified approach to the modeling of complex ice habits and recent studies have confirmed these spherical models are unable to accurately quantify ice scattering properties over a wide range of microwave frequencies (Petty and Huang 2010, Kulie et al. 2010). Accordingly, much work has been accomplished in recent years in characterizing the scattering properties of more realistic ice crystal shapes. As a result, many "scattering databases" are now available which provide key scattering parameters such as backscatter cross-section and extinction coefficient as a function of particle size for various ice habits (Hong 2007; Kim et al. 2007; Liu 2008b; Petty and Huang 2010). Of particular note are the results of Petty and Huang (2010), which is one of the first attempts to model the scattering properties of complex aggregate ice particles.

While these databases are an important step forward in realistically modeling ice particle properties and continue to be improved, if useful snowfall and ice parameters are to be derived one must still either (1) arbitrarily choose a single ice model to be representative of the population of ice particles under consideration or (2) average multiple ice models together to statistically account for the possible range of scattering properties. However, recent modeling work (Kneifel et al. 2011) has shown that by combining multiple radar frequencies it may be possible to obtain some ability to determine ice habit from radar reflectivity alone.

To date, little work has been accomplished considering a triple frequency approach and its potential benefits for snowfall retrievals. Yoshida et al. (2006) utilized a triple frequency approach to discriminate between different ice habits but considered only simple spherical and hexagonal ice particle models, required the accuracy of dual wavelength ratio (DWR) measurements to be better than 0.1 dB for the results to be useful, and only considered cirrus clouds. A triple frequency approach needs to be reconsidered in light of the more realistic ice particle models available today and with an emphasis on precipitation applications. Modeling results from Kneifel et al. (2011) show that the combination of Ku, Ka, and W-band frequencies could be key to gaining some ability to discriminate between ice habits, potentially providing a much-needed constraint on precipitation retrievals and thereby reducing their uncertainty.

However, these results have only been considered in the modeling realm and their implications have not yet been explored in observed data. The goal of this study is to explore observed triple-frequency signatures of snowfall and compare them to expectations from modeling, and consider the implications for snowfall rate retrieval techniques for current and future observation platforms.

Section 2 describes the triple-frequency radar data used in this study, and section 3 details the methodology used to calculate DWR from observed radar reflectivities. An analysis of the results in the triple-frequency framework is presented in section 4, and concluding remarks are given in section 5.

2. DATA

2.1 Scattering Databases

Kneifel et al. (2011) utilized pre-computed ice scattering model databases to calculate theoretical DWR results for a variety of ice habits assuming a simple exponential size distribution with a varying slope parameter. Interesting behavior was found when three common radar bands (Ku, Ka, and W) were considered. In particular, complex aggregate models were found to occupy a distinct region of this "triple-frequency" space compared to pristine particles and simple spherical models. Fig. 1 is an adaptation of this same approach, using scattering properties from two pre-computed databases.

The first database is Petty and Huang (2010), which consists of four models of aggregate snowflakes (DA1, DA2, DA3, NA). For the dendrite aggregate (DA1-DA3) models, a photograph of a single dendrite was digitized into a format suitable for Discrete Dipole Approximation (DDA) calculations. The single dendrite was then assembled stochastically with three different levels of complexity. The simplest model is DA1 and consists of only a few dendrites while the most complex is DA3 and consists of roughly ten. In addition, the needle aggregate (NA) model consists of multiple pristine needle particles assembled stochastically.

Second, scattering models of pristine crystals from Liu (2008b) were used. Specifically, various bullet rosette models (3BR-6BR), a sector snowflake (SEC), and a simple dendrite model (DEN) were included. Note, the behavior of these particles in triple frequency space is different from that of Kneifel et al. (2011) due to recent corrections made to the database (see Liu 2008b for information on obtaining this database). Using the

updated database, the Liu (2008b) particles now converge at low DWR. This is consistent with our expectations for the limit of Rayleigh scattering, indicating they are indeed more physically realistic.

Also, scattering properties for Mie spheres of various densities (MIE30-MIE200) and T-Matrix spheroids of various aspect ratios (T-MAT_0.5 – T-MAT_0.7) were computed as in Knefel et al. (2011).

Finally, an important difference in Fig. 1 compared to Kneifel et al. (2011) is in the choice of maximum particle sizes for the truncation of the SSD. The choice of maximum size is arbitrary but can have a significant impact. This choice is particularly important for the Liu (2008b) database because scattering calculations for unrealistic particle sizes are included in the database. For example, scattering properties for the bullet rosettes were calculated up to a maximum diameter of 10 mm, a size that would not be found in nature for this particle type. Though the final choice of a cutoff value is ad-hoc, a reasonable truncation value for Liu (2008b) particles was set at 5 mm. As a result, the Liu (2008b) particles exhibit a smaller maximum Ku-Ka DWR in Fig. 1 than in Kneifel et al. (2011).

On the other hand, aggregate snowflakes can grow to a centimeter or larger in nature, so sizes up to the maximum allowed by the Petty and Huang (2010) database were included in this study. The DA3 particle, for example, has a highest "effective" radius r_{eff} of 10 mm. In the case of a homogenous sphere, r_{eff} would equal the actual radius of the particle (Petty and Huang 2010).

Mie spheres were truncated at 5 mm and spheroids at 10 mm, though in these cases the choice of maximum size does not have a significant effect on triple-frequency behavior. For further discussion of the effects of truncation size, see Kneifel et al. (2011).

2.2 Wakasa Bay Observations

This work uses data from the 2003 Wakasa Bay AMSR Precipitation Validation

Campaign (Lobl et al. 2007). The Wakasa Bay dataset is uniquely applicable to this study

because it not only provides aircraft radar observations at the three frequencies considered by

Kneifel et al. (2011) but also includes data from a variety of snowfall events, ranging from

"widespread snow" to "light snow showers" (Lobl et al. 2007). Two radars were flown on

the NASA P-3 research aircraft: the scanning Airborne Precipitation Radar (APR) which

operates at 13.4 GHz (Ku-band) and 35.6 GHz (Ka-band) with a vertical resolution of 60 m,

and the nadir-only Airborne Cloud Radar (ACR) which operates at 94-GHz (W-band) with a

120 m vertical resolution (Table 1). Both radars also provide HH and HV polarization

information.

While the Wakasa Bay dataset is publicly available online from the National Snow

and Ice Data Center (NSIDC), this study utilizes a "beta" version of the radar observational

dataset that includes several calibration refinements and quality control improvements,

particularly to the APR observations. The beta dataset was created and provided by Dr.

Simone Tanelli of NASA's Jet Propulsion Laboratory (JPL).

A thorough exploration of the dataset was conducted to identify portions that would

be most amenable to analysis. A predominant mode of observed precipitation throughout the

Wakasa Bay campaign was stratiform rainfall was a readily identifiable bright band around

2-3 km. These cases are still useful for ice microphysical studies, however, because the

bright band can be identified (see section 3.4) and observations from within the bright band

or below can be discarded. Three days worth of these stratiform rainfall observations were

chosen for analysis: January 19 consisted of stratiform rainfall with some embedded

convection (see the top two panels of Fig. 2 for example W-band and Ku-band cross sections that are representative of this day's precipitation). January 23 consisted of lighter stratiform rainfall (Fig. 3). Finally, January 27 was notable for the particularly uniform appearance of the radar reflectivity structures (Fig. 4). As a result, this case became a focal point for analysis due to the expectation of well-behaved microphysical processes.

Two excellent oceanic snowfall cases were also observed during the Wakasa Bay campaign. The first was January 28 and consisted of shallow (2-3 km) snow showers (Fig. 5). The second was January 29 and consisted of deeper cloud top heights (4-5 km), higher reflectivities, and significantly more W-band attenuation (Fig. 6). Though coincident temperature information is unavailable, nearby soundings and 1000-500 hPa thickness charts were inspected to confirm that temperatures in the precipitating layers were below freezing. Of course, this does not discount the possibility of supercooled water and rimed particles, the effect of which will be discussed in later sections.

For each day considered, certain flight legs were discarded due to obvious quality control issues. In addition, only over-ocean data were considered due to difficulties with radar collocation over land (see section 3.1). The exact time ranges considered for each case are shown in Table 2.

3. METHODS

3.1 Collocation

Due to the differing resolutions and scanning characteristics of the two radars, collocation had to be performed to facilitate calculation of Ka-W DWR. A straightforward algorithm was used to accomplish this: for each ACR profile, find the near-nadir APR profile closest in time. Then for each ACR height bin, find the APR height bin from the time-collocated profile with the closest height, using the radar-based altitude (as opposed to aircraft pressure altitude) for both radars. Hence, the native ACR observations are used and the APR is collocated such that the collocated APR is on the same "grid" as the ACR. Also, note that the cross-track scanning APR observations have been discarded.

3.2 Attenuation Correction

As noted in, e.g., Hiley et al. (2011) and Kneifel et al. (2011), attenuation by liquid water and snowfall at cloud radar wavelengths is a significant issue, particularly at shorter (W-band) wavelengths. Given the nature of the precipitation events under consideration here, the impact of attenuation on DWR calculations clearly must be considered. This is more straightforward in the case of snow particles than for supercooled liquid water, because attenuation due to snow can be modeled and corrected for explicitly, though with some uncertainty. However, our lack of knowledge about amount and vertical distribution of supercooled liquid water means we are left to hypothesize about its effect.

Modeling results show that attenuation due to snow should be negligible at Ku and Ka band, but is potentially significant at W-band. Thus, we consider Ku-band "integrated

reflectivity" $Z_{int,Ku}$, simply the sum of reflectivity above a given height bin, increasing

downward from the aircraft:

$$Z_{int,Ku}(i) = \sum_{j=i}^{j=aircraft} Z_{linear,Ku}(j)$$

Integrated reflectivity (for the remainder of this paper, it is assumed that "integrated

reflectivity" refers to Ku-band) is plotted in Fig. 2 through Fig. 6 to give the reader an idea of

its behavior in a variety of situations. Note, the term "integrated reflectivity" is not

completely accurate due to the lack a factor *dz* accounting for vertical bin size; however, the

attenuation correction scheme presented in this section accounted for this properly and thus

produces physically consistent results.

$Z_{int,Ku}$ can be quantitatively related to W-band attenuation via the extinction

coefficients provided by the same scattering models used to calculate DWR. We chose to

consider only the more realistic pristine Liu (2008b) particles and Petty and Huang (2010)

aggregates. The exclusion of spheroid models is arbitrary but sensitivity tests showed their

inclusion did not have a significant impact on the analysis. An additional assumption must

be made for the SSD slope-intercept parameter N_o; however, this assumption was found to

have a minimal impact on calculations compared to choice of scattering model. Thus, N_o

was fixed at 10e7.

The results are shown in Fig. 7. The dense Liu (2008b) particles attenuate at W-band

more severely than the less dense Petty and Huang (2010) aggregates, illustrating the

inherent uncertainty in any attenuation correction scheme, with the spread in modeled W-

band attenuation increasing with increasing Ku-band integrated reflectivity. Thus, the exact

relationship used to correct W-band observations for attenuation is somewhat arbitrary. As a

result, we chose to simply use the average relationship for all models considered (the blue line in Fig. 7). The effect of this attenuation correction scheme is shown in Fig. 8 for the Jan. 27 case (bottom). All valid DWR points were overlaid on the triple frequency modeling results and colored by integrated reflectivity, such that the warmer colored points are subject to greater W-band attenuation correction. As expected, attenuation correction results in data points being shifted to the left on the triple frequency plot, due to inflated W-band reflectivities (and correspondingly reduced Ka-W DWR values).

A significant issue is that no direct information is available about the presence or quantity of supercooled water. Though passive microwave instruments were present on the aircraft that would have made liquid water content retrievals possible, unreliable instrumentation during the field campaign have made this infeasible (Simone Tanelli, personal communication, October 2011). So despite the potentially significant impact on these results, the effect of supercooled water must be inferred and considered a source of uncertainty in all the results presented here.

3.3 Smoothing

For optimal accuracy of DWR calculations, one would have radar reflectivity observations at every frequency looking at the exact same volume of air; i.e., the observations would have perfectly matched horizontal and vertical resolutions, and scan simultaneously. This is clearly not the case with the Wakasa Bay dataset due to mismatched beamwidths and vertical resolutions (Table 1), as well as mismatches in the timestamps of scans.

As a result, we experimented with a simple boxcar-average smoothing strategy in an attempt to provide a first-order correction for the effects of these resolution issues. The details are complicated slightly by the preprocessing applied to the ACR product: "Vertical profiles were recorded every 0.3 seconds and then averaged in post-processing to one profile every 3 seconds" (from the ACR documentation available online at http://nsidc.org/data/docs/daac/nsidc0212_rainfall_wakasa_acr.gd.html). So based on the vertical resolution differences between the APR and ACR, and manual inspection of the time resolution characteristics of each radar, smoothing was applied to the APR observations (before collocation), with a smoothing width of 3 temporally and 6 in the vertical.

Though admittedly simplistic, this smoothing algorithm has produced encouraging results, as shown in Fig. 8 (middle) for the Jan. 27 case. From Rayleigh scattering theory, both Ku-Ka and Ka-W DWR should go to zero for hydrometeors that are small compared to the radar wavelength. The scattering models shown in Fig. 1 agree with this prediction, generally converging at a DWR of zero for small size distribution slope parameters. This provides a useful constraint for analyzing whether our DWR calculations are physically realistic, because for small Ku-Ka DWR, the Ka-W DWR should approach zero. Since Fig. 8 shows an improvement in the amount of spread at small DWR, it appears that our smoothing algorithm is beneficial to the goal of reducing the amount of error due to beam mismatching that is inherent in this dataset. Thus, for the remainder of the paper the results will include smoothing.

3.4 Bright Band Identification

For the stratiform cases with clear bright bands, it was necessary identify the top of the bright band in order to only consider observations above the freezing level. An algorithm similar to Liao (2010) was used: starting at the bin nearest the aircraft and moving downward, the first occurrence of Ku-band Linear Depolarization Ratio (LDR) greater than -25 dB was considered to be the top of the bright band, and all data points at and below this level were discarded. For cases where the algorithm did not identify a bright band, the entire profile was discarded. Given the relatively small amount of data under consideration, it was possible to confirm that the algorithm produced reasonable results by visual inspection of cross sections of all the stratiform flight legs.

4. RESULTS

4.1 Jan. 27: Stratiform precipitation with obvious bright band

The results for the particularly uniform Jan. 27 stratiform case will be presented first. They are shown in Fig. 9 by overlaying all DWR data points on the triple frequency modeling results and coloring each point by it's Ku-band integrated reflectivity in order to illustrate both the amount of attenuation correction applied and to serve as a proxy for the distance of each data point from cloud top. Also shown in Fig. 9 is the corresponding normalized data density plot.

Initially, a striking feature of Fig. 9 is the peak in data density (bins containing more than 5% of all data points each) at low DWR. In terms of scattering models, this seems reasonable because it is in an area where several particles overlap each other, so one would expect a large number of points to fall in this DWR range. More simply, in the Rayleigh limit, DWR values should go to zero. Thus, for observations of primarily small particles we would expect a significant data density peak at small DWR.

Perhaps more interesting, however, are the multiple peaks into higher (greater than 5 dB) Ku-Ka DWR space. Though a relatively small number of data points comprise this feature, it is particularly interesting because only the Petty and Huang (2010) aggregate models overlap with these clouds of points. In addition, the data tends to be in agreement with the behavior of the scattering models at high Ka-W / low Ku-Ka DWR; i.e., the particle models under consideration successfully describe a bound on DWR values for the lower right portion of the triple frequency plot.

Also of note is the fairly smooth trend in integrated reflectivity with increasing DWR. Most points with an integrated reflectivity greater than 30 lie in an area of Ka-W DWR greater than about 8 dB and thus are better explained by the aggregate models. This is in agreement with a simple mental model of stratiform precipitation where pristine particles are formed at cloud top, with aggregation increasingly likely as particles fall deeper into the cloud (and therefore reach higher integrated reflectivities).

Likely the most notable triple-frequency feature of the Petty and Huang (2010) aggregate models is their distinctive "hook" shape at high values of Ku-Ka DWR. An important motivator of this study was to determine whether this hook feature can be found in observations. In this particular case, the scatter plot in Fig. 9 provides two hints of this hook shape, particularly for the needle and DA1/DA2 aggregates. However, the number of data points in these regions is relatively small, so it is difficult to draw conclusions based on this case alone; further analysis will be withheld until section 4.2.

4.2 Jan. 19 and Jan. 23: More stratiform rainfall with bright band at 2-3 km

Results for Jan. 19 are shown in Fig. 10 and for Jan. 23 in Fig. 11. While the results are quite similar for both cases, they are plotted in separate figures so that integrated reflectivity trends are not obscured. The location of peak frequency in the data density plots are shifted to the right compared to Jan. 27 and tend to overlap with the Mie, T-matrix, NA, and DA1 models more than the pristine Liu (2008b) particles. Given the increased reflectivities and embedded convection in these cases, it does seem plausible that pristine particles would be less predominant.

Quite striking in these two figures, in addition, is their behavior at high values of Ku-Ka DWR. Both cases exhibit the distinct "hook to the left" that the Petty and Huang (2010) models suggest. In particular, the observations follow NA and DA3 quite well. Once again, the number of data points in this region of large Ku-Ka DWR is quite small compared to the total number of observations under consideration. However, the presence of the hook feature in all stratiform cases considered is clear evidence for realistic nature of this particular feature of the Petty and Huang (2010) models.

4.3 Jan. 28: 2-3 km deep snow showers

Fig. 12 shows the results for the shallow snow showers of Jan. 28. Again quite striking is the location of the peak in data density. Instead of occurring in the low DWR space occupied primarily by Liu (2008b) particles, for this case it occurs at relatively high DWR in an area occupied exclusively by the aggregate models. Comparing this case to the results for Jan. 27, the observations suggest that the Jan. 27 stratiform case consists mostly of smaller ice particles that are more likely to be pristine, while the Jan. 28 case consists of larger particles that are more likely to be aggregated snowflakes. The agreement in these observations with a simple mental picture of convective situations being dominated by aggregation while stratiform precipitation will consist of smaller, pristine particles is an exciting result of this work and will be discussed further in the conclusion.

4.4 Jan. 29: 4-5 km deep snow

Finally, Fig. 13 shows the results for the deeper Jan. 29 snowfall case with cloud tops as high as 5 km. Here, the location of peak data density occupies a region in

between those of the Jan. 27 stratiform case and the Jan. 28 light snow shower cases. However, the amount of spread and number of outliers in this case appears to be an indication that deep, heavy, convective snowfall amplifies almost all the issues and sources of uncertainty associated with the study. The high spatial variability of intense, convective snow will amplify imperfect beam-matching and any small collocation problems. In addition, the convective updrafts are more likely to contain large amounts of supercooled water, causing greater attenuation at W-band than would be accounted for by our consideration of attenuation by snow alone. Thus, it is difficult to draw many conclusions from this case but it is still useful in that it illustrates many of the caveats of this study.

5. CONCLUSIONS

Despite the multitude of challenges associated with this dataset, such as attenuation at W-band, our lack of ability to quantify the effect of supercooled water, imperfect collocation, and beam-matching issues, several useful conclusions can be drawn.

First, a large number of data points have a DWR signature that can only be explained by aggregate models. For the Jan. 27 case in particular, the maximum frequency of occurrence occurs in the aggregate region of the triple frequency plots. Perhaps more importantly, the stratiform cases consistently demonstrate the characteristic hook shape of the Petty and Huang (2010) aggregate models, with Ka-W DWR trending back toward the negative direction as Ku-Ka DWR becomes large. This is significant because it provides a result that is insensitive to a potentially major issue with the current methodology: the results are quite sensitive to the calibration of the ACR relative to the APR. Specifically, while the absolute location of maximum frequency in triple frequency space is sensitive to discrepancies in radar calibration, the hook back toward smaller Ka-W DWR will be preserved even if the ACR calibration is changed relative to the APR. In other words, in triple frequency space, a hypothetical increase in W-band calibration would only serve to shift the observations to the left in triple frequency space; however, their shape would be preserved. This is an important result because it shows that the unique triple-frequency behavior of the Petty and Huang (2010) scattering models can in fact be found in observations. This is an indicator that the current trend toward the development of increasingly complex and realistic snowflakes is both useful and necessary.

The finding that the Petty and Huang (2010) aggregates are crucial for explaining triple-frequency observations also has implications for current and near-future snowfall rate

retrieval algorithms. Simple algorithms based on single and dual frequency radar reflectivity observations, such as those from CloudSat and the upcoming Global Precipitation Measurement (GPM) mission, should consider incorporating the latest aggregate models in the derivation of radar reflectivity-snowfall rate relationships. Perhaps more important is in the realm of passive microwave radiative transfer calculations, where accurate scattering properties across a range of frequencies is particularly important. This work serves as further evidence that simple Mie-scattering based calculations of microwave scattering properties are insufficient. In addition, it appears that of currently available scattering models, the Petty and Huang (2010) aggregates may be the best "default" choice, due to (a) their realistic behavior across multiple frequencies compared to e.g., Mie spheres, and (b) their enhanced ability compared to Liu (2008b) particles to accurately represent larger particle size ranges that are more representative of snowfall found in nature.

Next, some interesting microphysical inferences can be made by comparison of the Jan. 27 and Jan. 28 cases. The stratiform precipitation of Jan. 27 exhibits a large proportion of DWR observations in the region where several models overlap, particularly the pristine Liu (2008b) particles, suggesting that this snowfall event was comprised primarily by small, and likely pristine, ice particles. By contrast, observations of the more convective snow showers of Jan. 28 have predominantly larger values of DWR and primarily occupy the region of triple frequency space covered by the Petty and Huang (2010) models. This an apparent confirmation of our general expectation that convective snow showers would be comprised primarily of larger aggregated particles while light stratiform precipitation would have a larger quantity of smaller, pristine particles. These broad distinctions hint at the

potential utility of a triple frequency approach to retrieving snowfall parameters like ice habit and some properties of the size distribution for future observation platforms.

This work also leads to several avenues of future research. Ground-based multi-frequency radar observations, such as those from the Department of Energy's Atmospheric Radiation Measurement (ARM) facilities, would be particularly useful. Given the lesser impact of attenuation near the surface and lack of ground clutter issues, ground-based observations would allow for a clearer analysis of multi-frequency observations at the lowest 1-2 km, where important processes such as near-surface aggregation are still poorly understood. In addition, ground-based datasets have other potential benefits such as longer-term seasonal and yearly datasets which would provide more robust statistics and a wider variety of snowfall cases. Recent field campaigns such as the GPM Cold-Season Precipitation Experiment (GCPEx) should also be explored for potential multi-frequency studies, and future field campaigns should be aware of the utility of collocated multi-frequency observations as they consider their instrumentation and scanning strategies.

Various methodology details can also be explored, particularly the effect of more realistic particle size distributions. Finally, as work on developing increasingly realistic and complex snowflake scattering models continues, the latest models can be incorporated into this triple frequency modeling framework, which will no doubt add further insights to this analysis.

REFERENCES

Bennartz, R., and G. W. Petty, 2001: The sensitivity of microwave remote sensing observations of precipitation to ice particle size distributions. *J.Appl.Meteorol.,* **40**, 345-364.

Choi, G., D.A. Robinson, and S. Kang, 2010: Changing Northern Hemisphere Snow Seasons. *J. Climate*, **23**, 5305-5310.

Hiley, M.J., M.S. Kulie, and R. Bennartz, 2011: Uncertainty analysis for CloudSat snowfall retrievals. *J. Appl. Meteor. Climatol.,* **50**, 399-418.

Hinzman, L. D., and Coauthors, 2005: Evidence and implications of recent climate change in northern Alaska and other Arctic regions. *Climatic Change*, **72**, 251–298.

Hong, G., 2007: Radar backscattering properties of nonspherical ice crystals at 94 GHz. *J. Geophys. Res.,* **112**, D22203, doi:10.1029/2007JD008839.

Kim, M.-J., M. S. Kulie, C. O'Dell, and R. Bennartz, 2007: Scattering of ice particles at microwave frequencies: A physically based parameterization. *J. Appl. Meteor. Climatol*., **46**, 615–633.

Kneifel, S., M.S. Kulie, and R. Bennartz, 2011: A triple frequency approach to retrieve microphysical snowfall parameters. *J. Geophys. Res.-Atmospheres,* **116**, D11203, doi:10.1029/2010JD015430.

Kulie, M.S., and R. Bennartz, 2009: Utilizing space-borne radars to retrieve dry snowfall. *J. Appl. Meteor. Climatol.*, **46**, 615-633.

Kulie, M.S., R. Bennartz, T. Greenwald, Y. Chen, and F. Wenig, 2010: Uncertainties in microwave optical properties of frozen precipitation: Implications for remote sensing and data assimilation. *J. Atmos. Sci.,* **67**, 3471-3487.

Liao, L., and R. Meneghini, 2011: A study on the feasibility of dual-wavelength radar for identification of hydrometeor phases. *J. Appl. Meteor. Climatol.*, **50**, 449-456.

Liu, G., 2004: Approximation of single scattering properties of ice and snow particles for high microwave frequencies. *J. Atmos. Sci.*, **61,** 2441-2456.

Liu, G., 2008a: Deriving snow cloud characteristics from *CloudSat* observations. *J. Geophys. Res.*, **113**, D00A09, doi:10.1029/2007JD009766.

Liu, G., 2008b: A database of microwave single-scattering properties for nonspherical ice particles. *Bull. Amer. Meteor. Soc.,* **89**, 1563–1570.

Lobl, E.S., and Coauthors, 2007: Wakasa Bay - an AMSR precipitation validation campaign. *Bull. Amer. Meteor. Soc.,* **88**, 551-558.

Luckman, A., T. Murray, R. de Lange, and E. Hanna, 2006: Rapid and synchronous ice-dynamic changes in East Greenland. *Geophys. Res. Lett.*, **33**, L03503, doi:10.1029/2005GL025428.

Matrosov, S. Y., 2007: Modeling backscatter properties of snowfall at millimeter wavelengths. *J. Atmos. Sci.*, **64**, 1727–1736.

Molthan, A.L., and W.A. Petersen, 2011: Incorporating Ice Crystal Scattering Databases in the Simulation of Millimeter Wavelength Radar Reflectivity, *J. Atmos. Oceanic Technol.,* **28**, 337-351.

Petty, G. W., and W. Huang, 2010: Microwave Backscatter and Extinction by Soft Ice Spheres and Complex Snow Aggregates, *J. Atmos. Sci.*, **67**, 769-787.

Yoshida, Y., Asano, S., and K. Iwanami, 2006: Retrieval of microphysical properties of water, ice, and mixed-phase clouds using a triple-wavelength radar and microwave radiometer, *J. Meteorol. Soc. Jpn.*, **84**, 1005-1031.

TABLES

	APR2 Ku-band	APR2 Ka-band	ACR W-band
Frequency (GHz)	13.405	35.605	94
3-dB beamwidth (°)	3.8	4.8	0.8
Vertical resolution (m)	60	60	120

Table 1

Relevant instrument characteristics for APR2 and ACR radars. See Lobl et al. (2007) for more detailed specifications.

Group	Observation Time Ranges (UTC)	Number of DWR points
Jan 19 Stratiform with embedded convection	03:45-05:18 05:26-06:19 07:35-09:20	31,514
Jan 23 Stratiform	06:41-10:51	44,239
Jan 27 Light Stratiform	03:30-06:25	24,093
Jan 28 Shallow snow	03:52-04:59 05:05-05:25 05:39-07:09	12,417
Jan 29 Deep snow	03:15-06:24	50,517

Table 2

Exact time ranges and number of DWR points for each case.

FIGURES
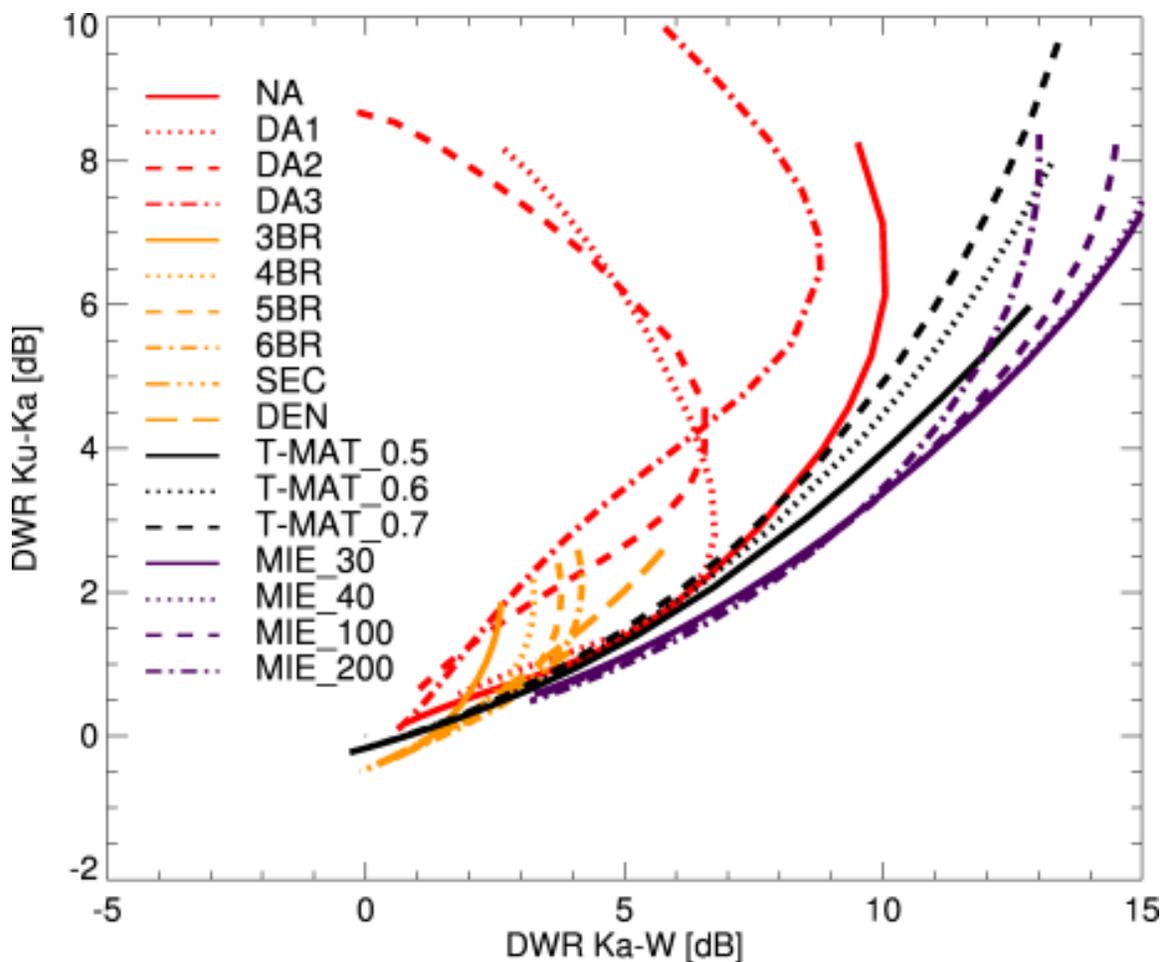
Fig. 1

Triple-frequency DWR calculations for various ice particle scattering models: Needle Aggregate (NA) and Dendrite Aggregates (DA1-DA3) from Petty and Huang (2010); Bullet Rosettes (3BR-6BR), Sector (SEC), Dendrite (DEN) from Liu (2008b); T-matrix spheroids for aspect ratios of 0.5, 0.6, and 0.7 (T-MAT_0.5-T - MAT_0.7); Mie spheres with density varying from 30 kg m^{-3} to 200 kg m^{-3} (MIE_30 – MIE_200). Adapted from Kneifel et al. (2011) (see section 2.1 for a summary of key differences).
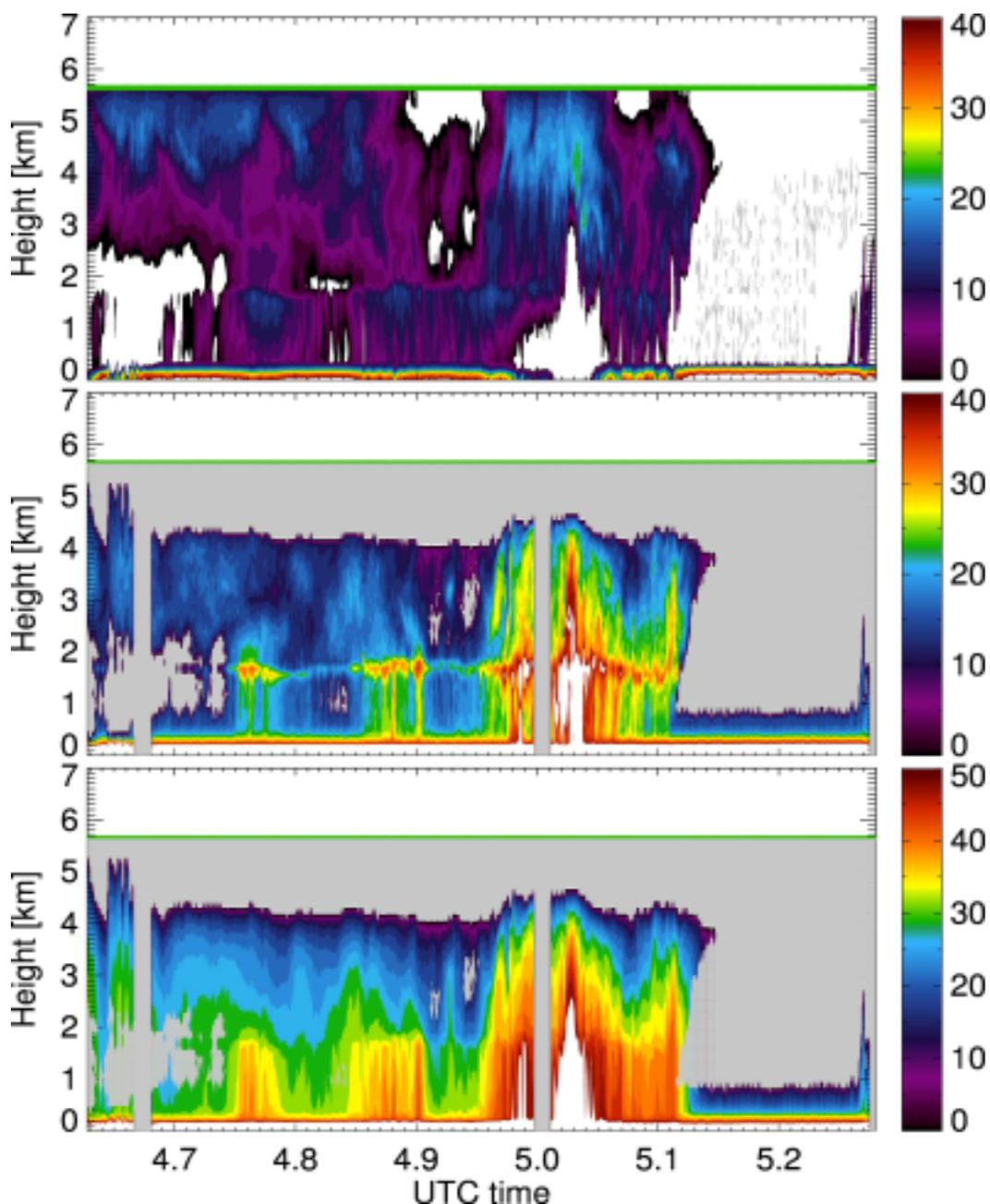
Fig. 2

Example cross sections from the January 19 case. Note, this is only a subset of the January 19 data and was chosen as representative of observations from that day. Top: W-band reflectivity with no attenuation correction [dBZ]. Middle: Ku-band reflectivity with no smoothing, collocated to W-band [dBZ]. Bottom: Integrated Ku-band reflectivity [dBZ$_{int}$]. Gray shading represents either missing data or observations that were rejected due to collocation issues; white indicates that the observations are either greater or less than the range of the color scale. The horizontal green line represents the altitude of the aircraft.
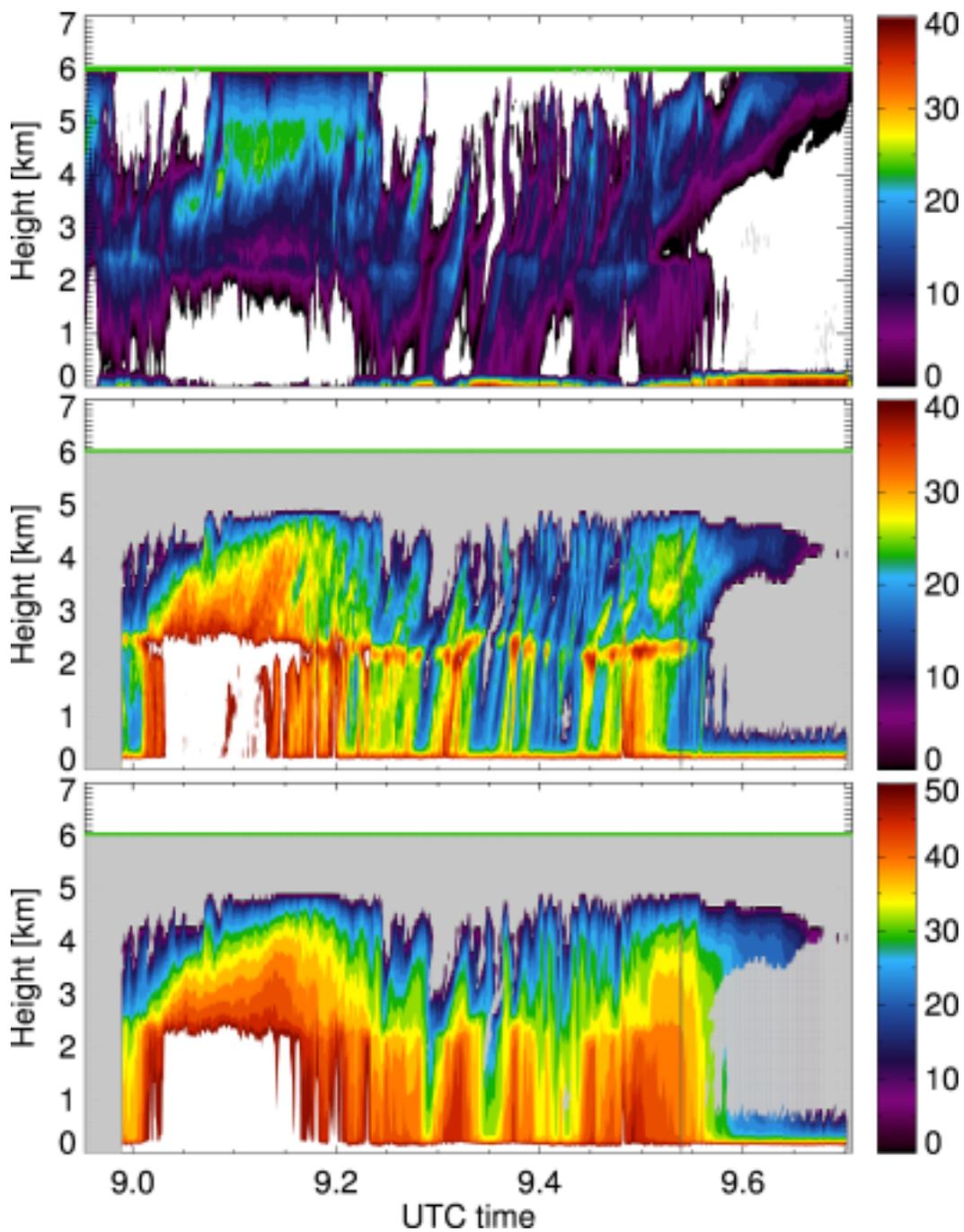
Fig. 3

As in **Fig. 2**, but for January 23 case.
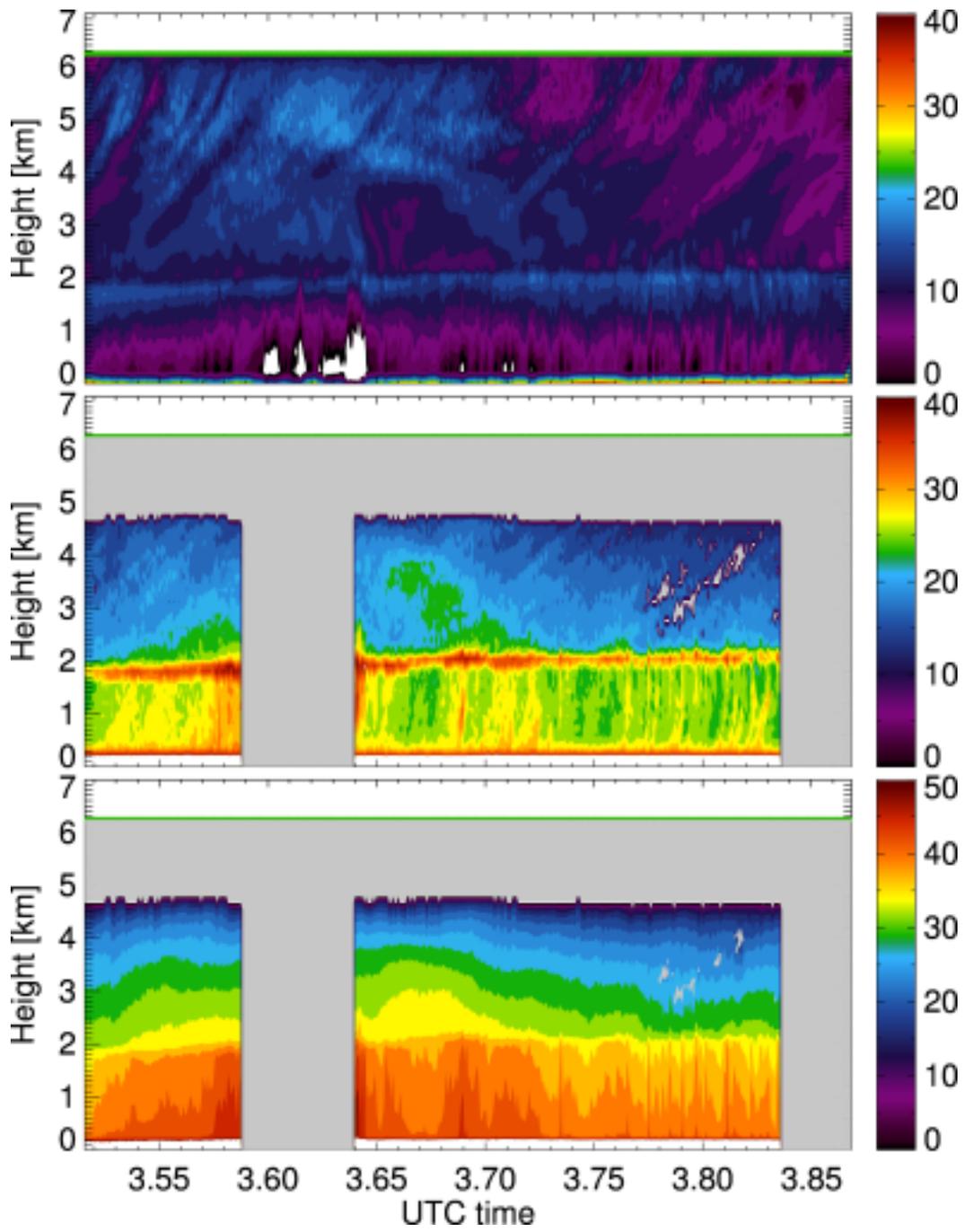
Fig. 4

As in **Fig. 2**, but for January 27 case.
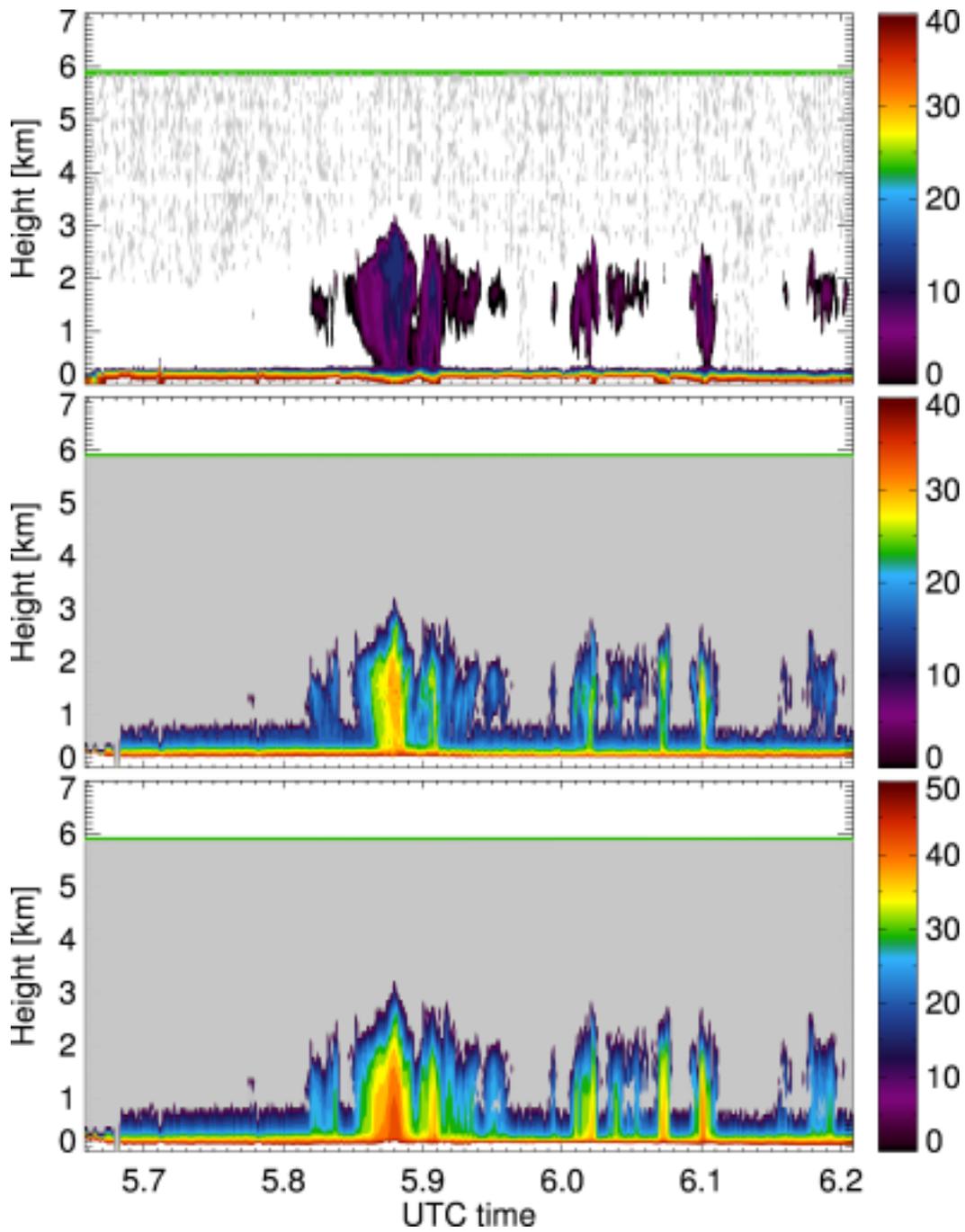
Fig. 5

As in **Fig. 2**, but for January 28 case.
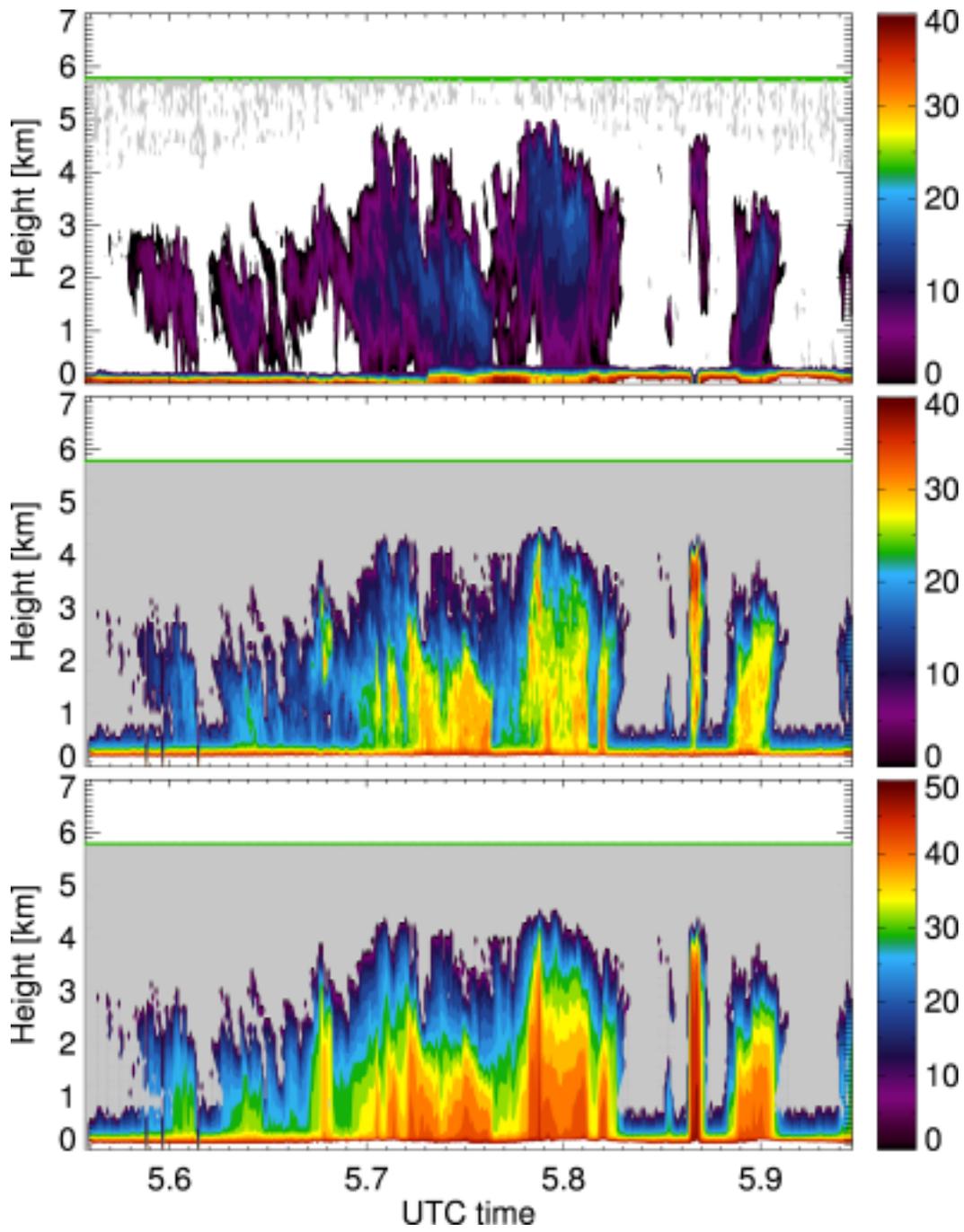
Fig. 6

As in **Fig. 2**, but for January 29 case.
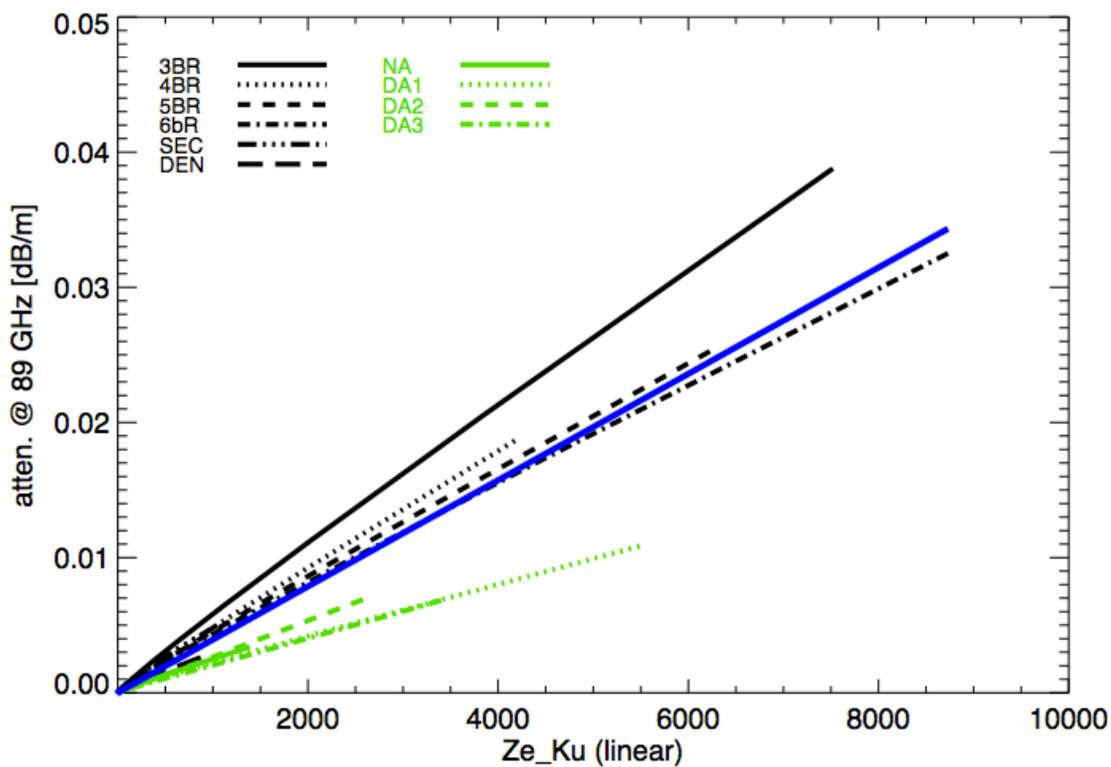
Fig. 7

Relationship between integrated Ku-band reflectivity and attenuation at W-band for Liu (2008b) particle models (black lines) and Petty and Huang (2010) aggregate models (green lines). The blue line is the average of all models shown in this plot. Model abbreviations are the same as Fig. 1.
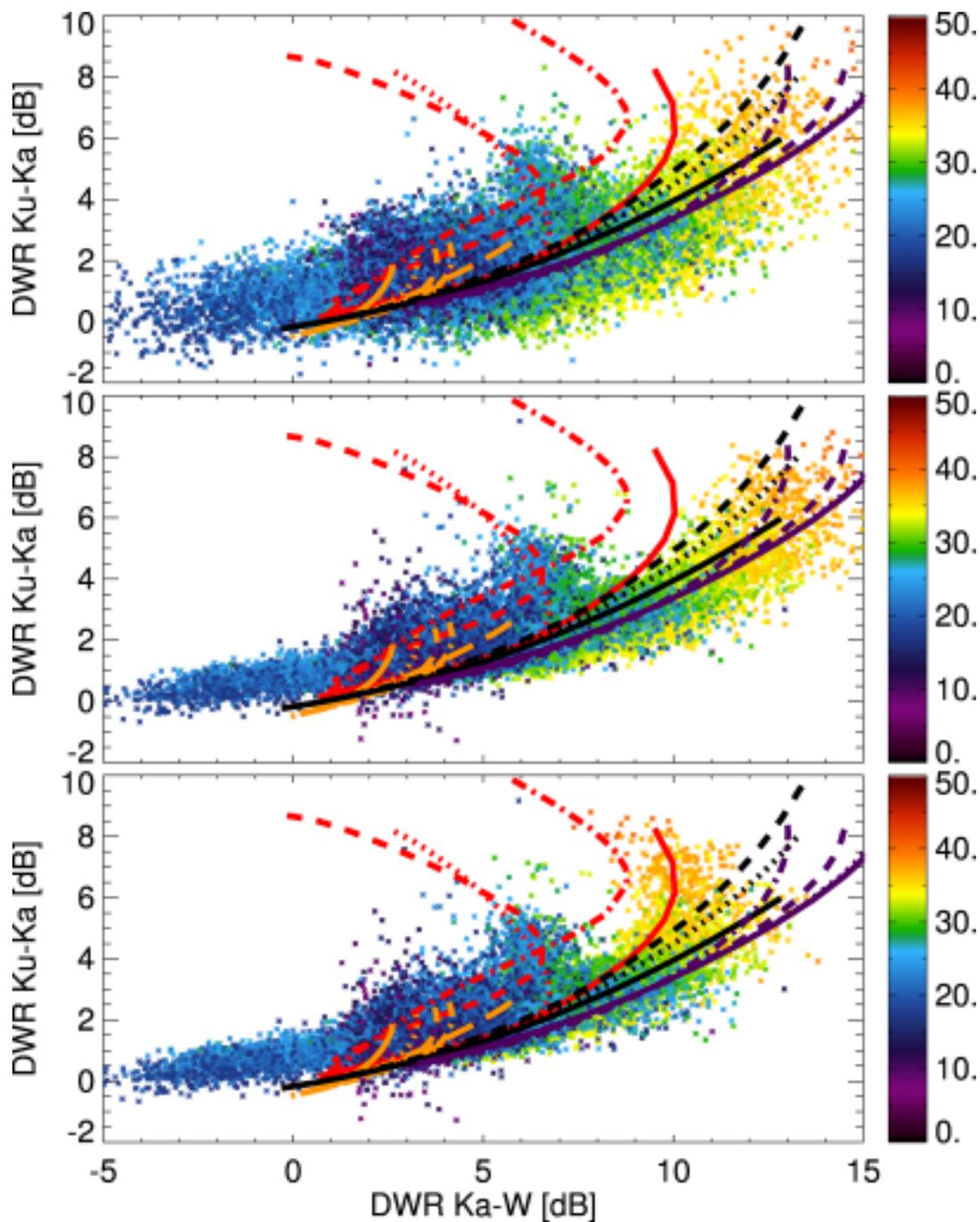
Fig. 8

Computed DWR values for January 27 case. Scatter points are colored by integrated reflectivity. Ice models are overlaid as in **Fig. 1**. Top: no smoothing, no attenuation correction. Middle: With smoothing, no attenuation correction. Bottom: With smoothing, with attenuation correction.
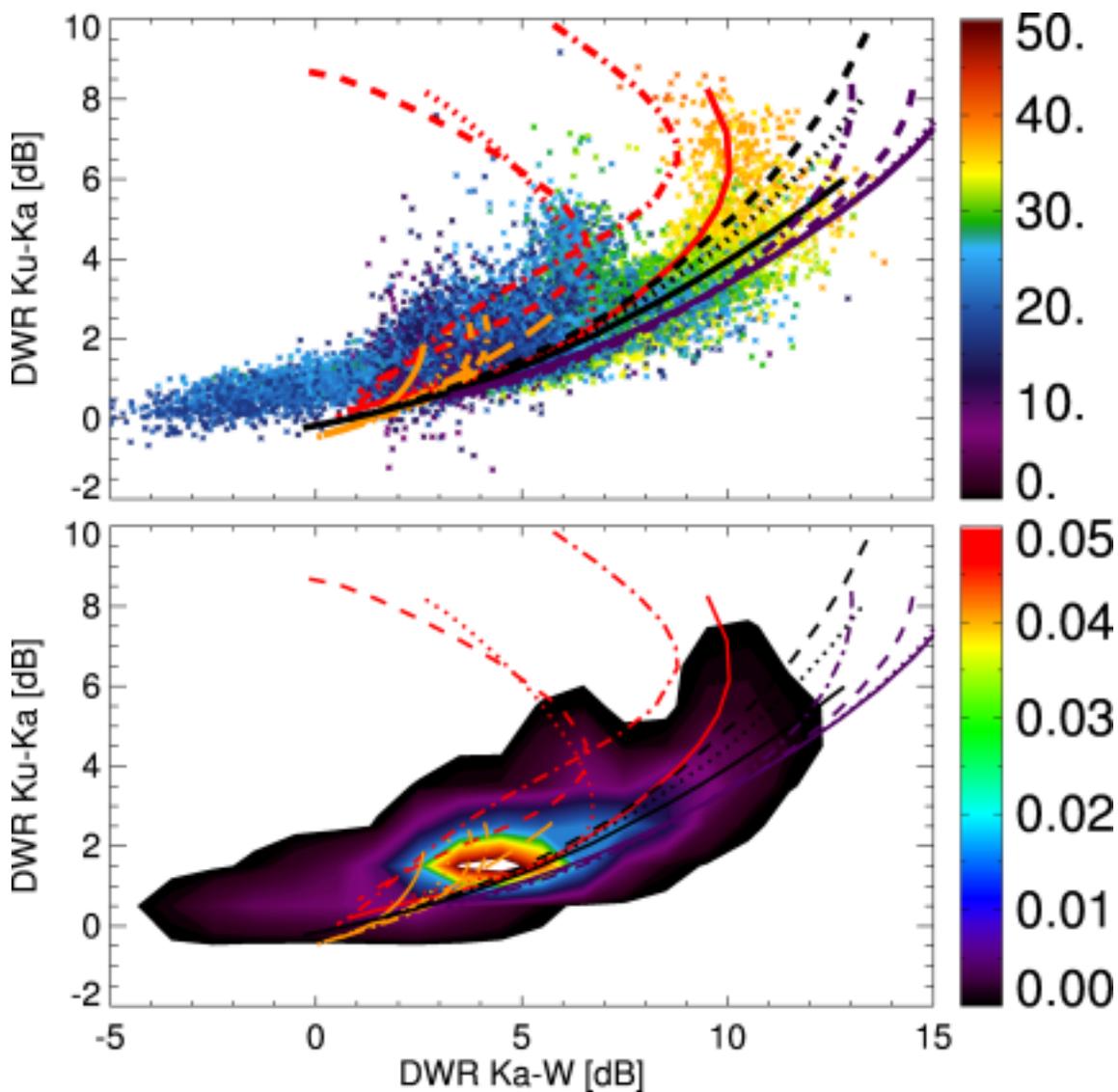
Fig. 9

Results for January 27 case (light stratiform precipitation), with APR smoothing and W-band attenuation correction (see Table 2 for exact time ranges and number of points). Top: as in **Fig. 8** bottom. Bottom: Normalized frequency of occurrence in 1 dB x 1 dB bins.
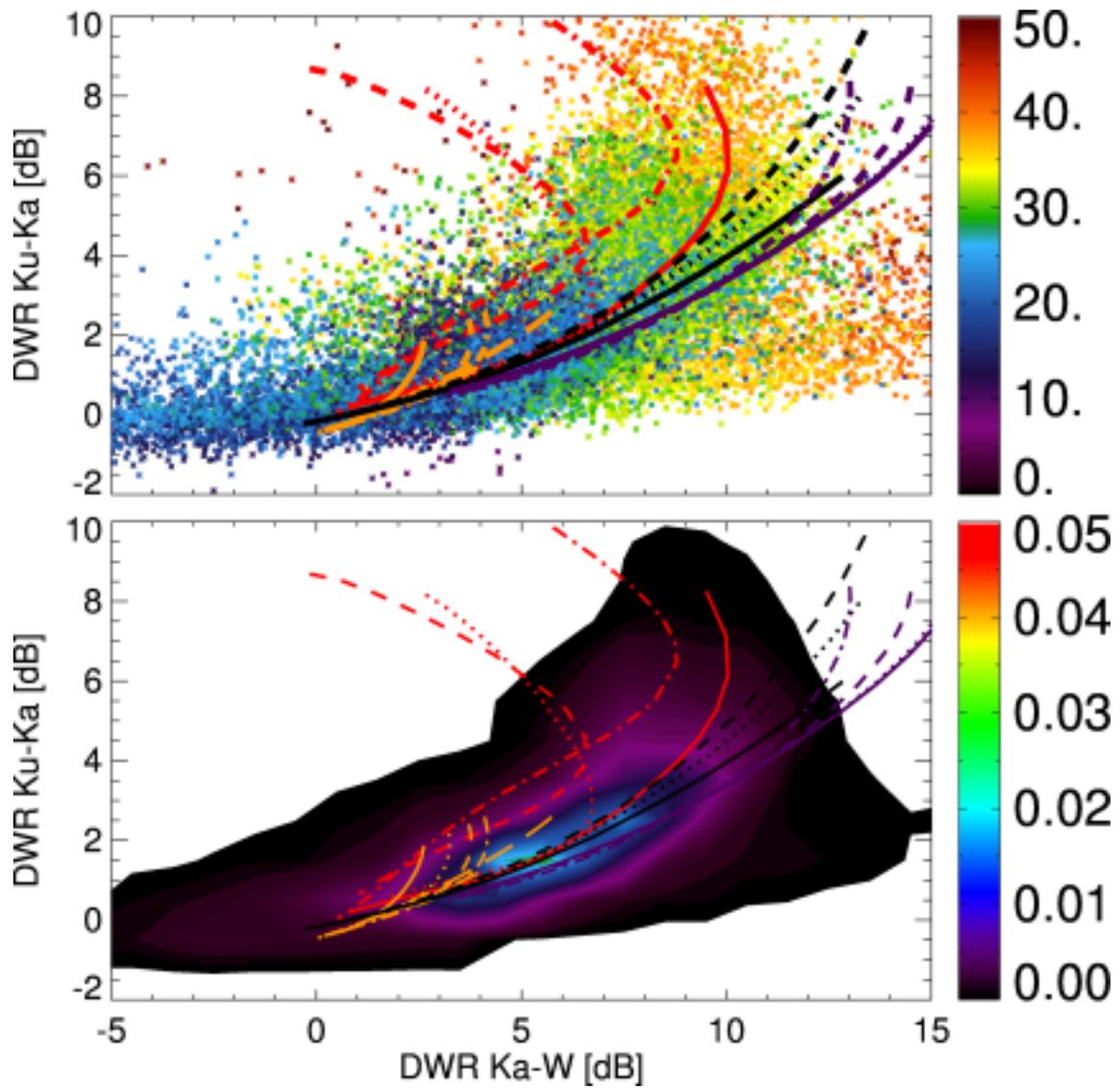
Fig. 10

As in **Fig. 9**, but for January 19 case (stratiform precipitation).
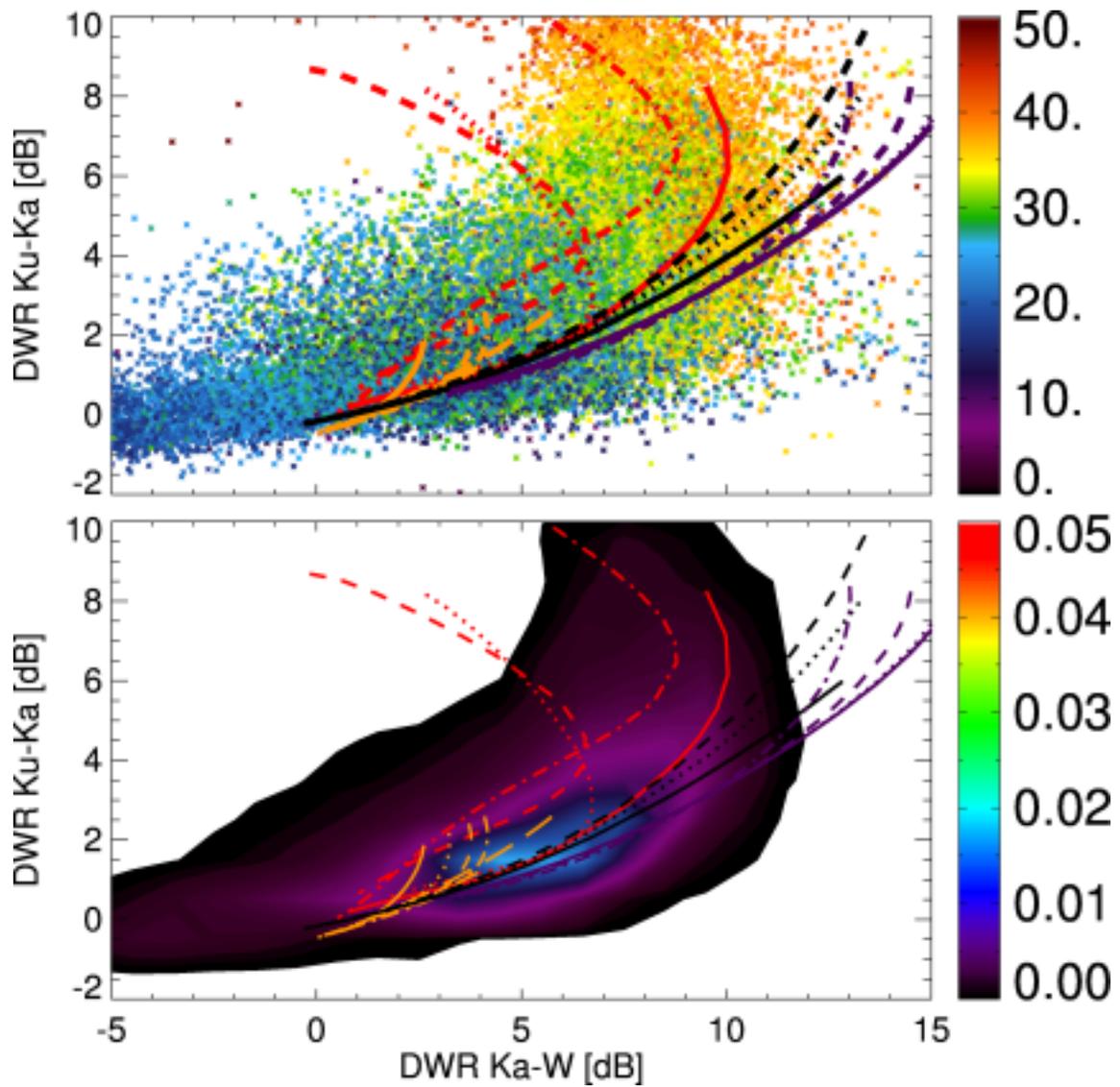
Fig. 11

As in Fig. 9, but for January 23 case (stratiform precipitation).
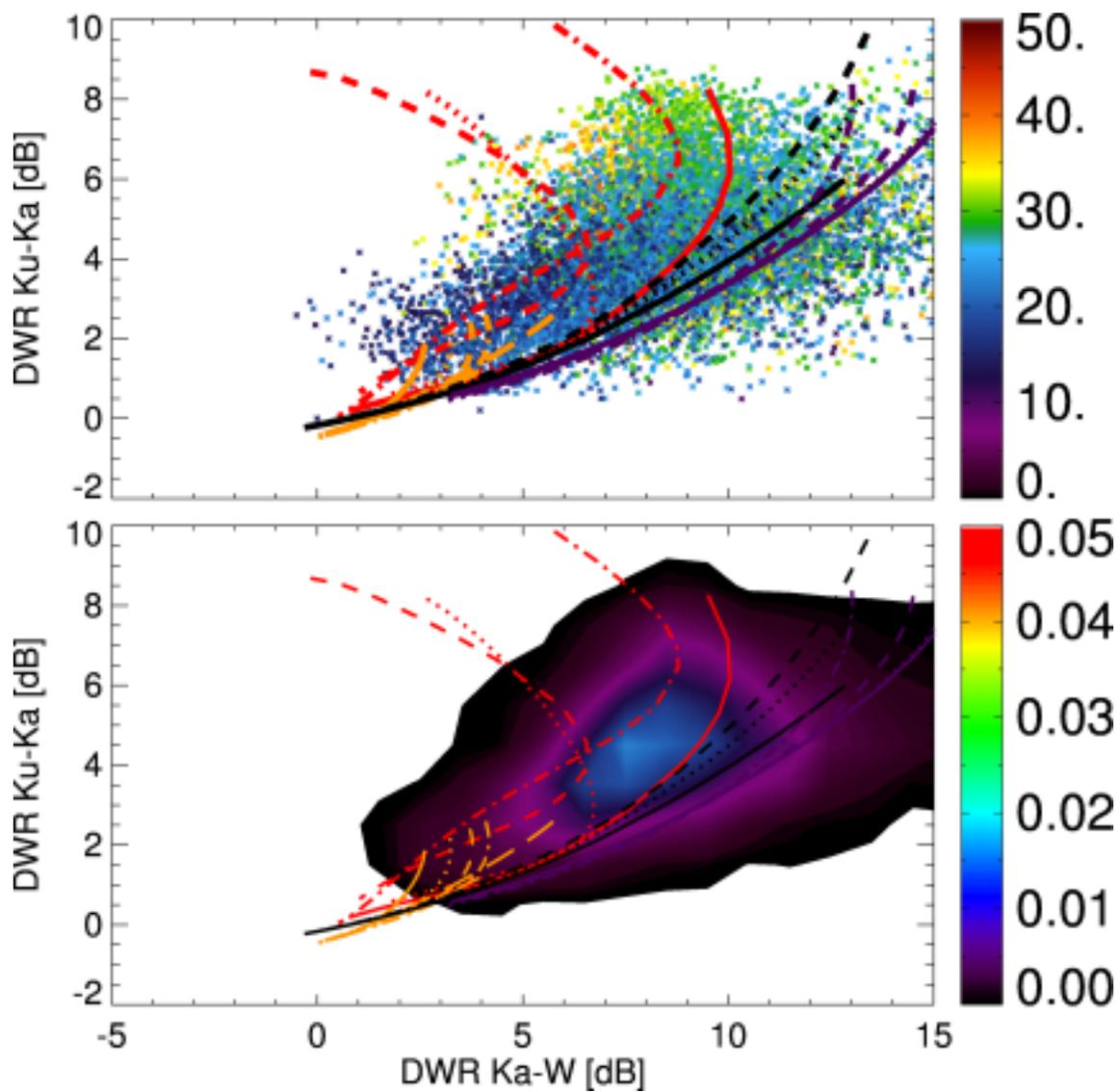
Fig. 12

As in **Fig. 9**, but for January 28 case (shallow snow showers).
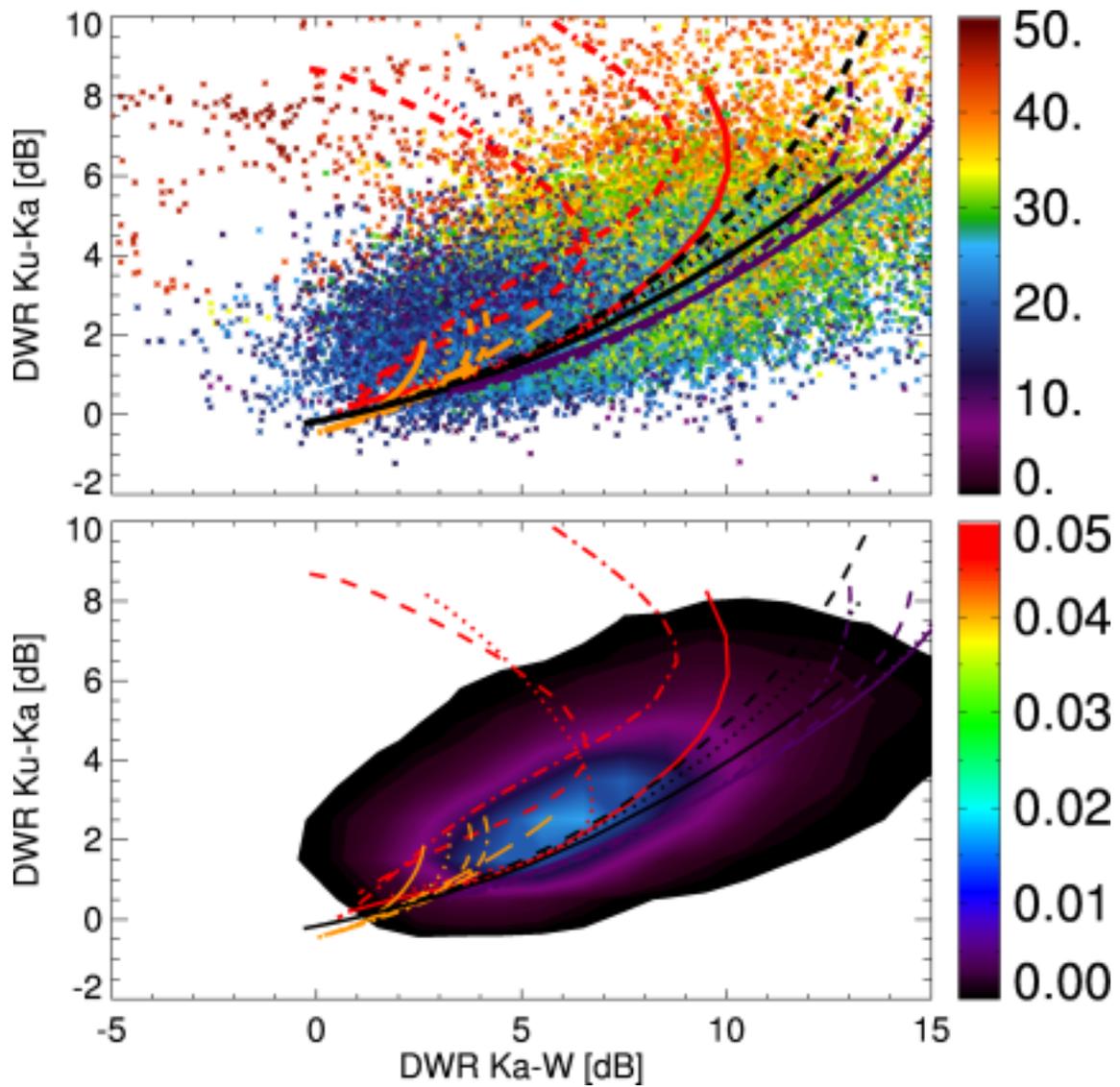
Fig. 13

As in Fig. 9, but for January 29 case (deep convective snowfall).